Detection of chemical nutrients in water using a fluidic microplasma chip with enhanced optical collection efficiency

by

Shenmin Gong

A thesis submitted to the graduate faculty

In partial fulfillment of the requirement for the degree of

MASTER OF SCIENCE

Major: Electrical Engineering

Program of Study Committee
Long Que, Major Professor
Qiao Daji
Ian Schneider

The student author, whose presentation of the scholarship herein was approved by the program of study committee, is solely responsible for the content of this thesis. The Graduate College will ensure this thesis is globally accessible and will not permit alterations after a degree is conferred.

Iowa State University

Ames, Iowa

2018

DEDICATION

I would like to dedicate this thesis to my parents Hongbin Gong and Weihong Mao. Without their unconditional love and financial support, I would not have been able to complete this work.

TABLE OF CONTENTS

LIST OF FIGURES

ACKNOWLEDGEMENTS

I would like to express the deepest appreciation to my major professor, Long Que, and committee members, Daji Qiao and Ian Schneider. Without their help, I would not have achieved my goal.

I would like to thank our research group members: Chao Song, Xiangchen Che, Silu Feng, Zhichong Yu, Xiaoke Ding, Rengyuan Yang, Subin Mao. Thanks for their support and advices.

I would like to thank all of my friends who stay with me during my master period.

Finally, I must say thanks to my family members.

ABSTRACT

This thesis reports the results of projects I have participated in during the period of my masters' thesis. The first project reports a new fluidic micro-plasma chip with an Al-coated spherical surface. This device is designed to efficiently capture the glowing microdischarge signal. The detection of nutrients in water using this chip has been demonstrated. The detailed explanations of the basic principle of glowing microdischarge signal, the fluidic microplasma chip, the operating optical system, the concentration tests and result data analysis will be introduced in the following chapters. We detected the nitrate and phosphate in water sample successfully with our device.

The second project reports an optimized microfluidic droplet device for fabricating 3D microtissues and studying the cell behaviors in 3D microtissues. It has been found by properly selecting the size of the microchambers on the microfluidic device and choosing an optimal concentration of collagen to fabricate microtissues. The behaviors of cells in the microtissues can be essentially the same as those of cells in a conventional cell culture system. Furthermore, this optimized microfluidic droplet device for fabricating 3D collagen-based microtissues can also be used to study breast cancer cell proliferation and motility. This is additional work that I did for my master's thesis and is included in the appendix.

CHAPTER 1. GENERAL INTRODUCTION

Thesis Organization

This thesis starts by describing the research project "Detection of Chemical Nutrients in Water Using a Fluidic Microplasma Chip with Enhanced Optical Collection Efficiency", which has been published as a proceeding from MicroTAS conference. Chapter 2 also includes the basic principle of glowing micro-discharge signal, the fluidic micro-plasma chip, the operating optical system and result data analysis.

Appendix A describes the research project related to cells' behaviors in a microfluidic device. This Appendix includes two papers "High Throughput Studies of Cell Migration in 3D Microtissues Fabricated by a Droplet Microfluidic Chip" (published in Micromachines) and "Studies of Cell Behaviors in 3D Microtissues in Microfluidic Device: Growth and Migration" (published on IEE sensors conference 2017). It included the description of the microfluidic device, device fabrication, experimental producers, experiment result data and discussions on the studies of cell behaviors.

Appendix B is the mask schematics and its design function.

Appendix C is the materials and surface functionalization.

Appendix D is the AAO fabrication.

CHAPTER 2. DETECTION OF CHEMICAL NUTRIENTS IN WATER USING A FLUIDIC MICROPLASMA CHIP WITH ENHANCED OPTICAL COLLECTION EFFICIENCY

Modified from a paper published in MicroTAS 2017

Shenmin Gong, Chao Song, Daji Qiao and Long Que

Abstract

This paper reports a new fluidic microplasma chip with an Al-coated spherical surface designed to capture the glowing microdischarge signal. The detection of nutrients in water using this chip has been demonstrated. Compared to conventional techniques (UV/Vis spectrometry, ion chromatography, high-performance liquid chromatography, and capillary electrophoresis), this new fluidic microplasma chip offers many advantages such as low cost, small size, simple measurement procedures and detection of multiple species. Experiments found that nitrate and phosphate can be detected by this fluidic microplasma device simultaneously. A sample's concentration can also be measured by using the intensity of the nitrogen spectrum which are seen in the microdischarge. As the sample's concentration increases, the spectra intensity of the water sample increases.

Introduction

Water is one of the most common chemicals on earth. It is an important resource for the survival of all living things. In addition, all living things are composed primarily of water. Many biochemical reactions occur in water, and it is used to fill the spaces in and between cells. In the human body, water is also necessary for digestion, absorption, transport, nutrient dissolution, etc.

The importance of water to living creatures, particularly human, has led to the concern about water pollution. The technologies leading to the design of water quality sensors to detect the chemicals in water have been the focus of research for years. However, a large amount of work still is to be completed in order to improve a sensor's specificity, accuracy and concentration limitations.

Water quality testing is also an important part of environmental monitoring. Water quality affects the surrounding ecosystem. Several parameters are used to characterize the water quality. Important measures of chemical characteristics of water quality include pH, dissolved oxygen, disinfectant concentration, nitrogen content (ammonia, amines, nitrate) and phosphorous content (phosphate). We will mainly discuss the following parameters: nitrogen and phosphorous.

Nitrogen is the most abundant chemical element in the air. Nitrogen is rare in the earth's crust. Most of it is present in the atmosphere in the form of diatomic nitrogen molecules, which makes up about 78% of earth's atmosphere. However, nitrogen in the gaseous form cannot be absorbed and used as a nutrient by plants and animals. The process of converting N_2 into ammonia and other nitrogenous is called nitrogen fixation[***Fig.1***].

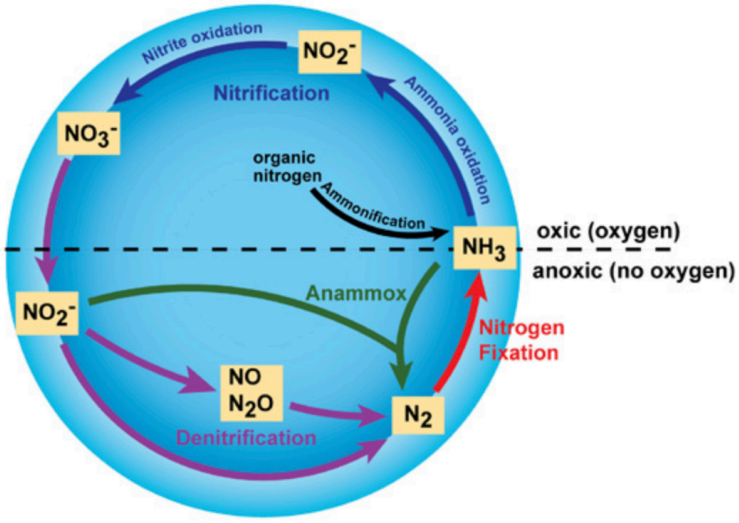

Figure 1: Major transformations in the nitrogen cycle

In nature, there are two ways to fix nitrogen. First, nitrogen fixation by lightning, high temperature discharge, etc. This formation of nitrogen fixation is rare. The second way is biological nitrogen fixation; that is, the diatomic nitrogen molecules are reduced to highly water-soluble ammonia within biological organisms, mainly microorganisms. The basic reactions of nitrogen-fixing microorganisms is as follow:

$$N_2 + 8H^+ + 8e^- + 16\ ATP + 16\ H_2O \rightarrow 2\ NH_3 + H_2 + 16\ ADP + 16\ Pi$$

The following basic conditions must be met in order for this reaction to proceed: nitrogen-fixing enzymes must be available; there must be electron donors; there must be an energy supply (since N_2 molecule has a strong bond with high bond energy and it requires lots of energy to break it); the environment is free from oxygen, due to the fact that the enzyme that catalyzes nitrogen fixation is usually inhibited by oxygen.

After the nitrogen is converted to ammonia, the process of converting ammonia to nitrite and nitrate is also an important step in the global cycle. A two-step chemical reaction is carried out in this process. First, the oxidation of ammonium(NH_4^+) to nitrite(NO_2^-):

$$2NH_4^+(aq) + 3O_2(g) \rightarrow 2NO_2^-(aq) + 2H_2O(l) + 4H^+(aq)$$

Second, the oxidation of nitrite(NO_2^-) to nitrate(NO_3^-):

$$2NO_2^-(aq) + O_2(g) \rightarrow 2NO_3^-(aq)$$

Nitrate, nitrite and ammonium are important factors in water quality detection. Many reviews have discussed the design and fabrication of nitrate and nitrite sensors [1-3]. Excessive concentrations of nitrate, nitrite and ammonium in the soil will cause water loss in plants eventually leading their death. For these reasons, the maximum allowable contaminant level for nitrate-

nitrogen has been set at 10 ppm (10 mg L^{-1} or 0.7 mM) by the U.S. Environmental Protection Agency (EPA).

Phosphate is a naturally occurring form of the elemental phosphorus that can be found in various phosphorous-containing minerals. In organisms, phosphorus appears in form of free phosphate ions. Phosphorous is a crucial nutrient for plant growth. The ***Fig. 2*** shows the eutrophication of a lake, the eutrophication means the nutrients in a lake or other body of water are rich. The excessive phosphate will boost the phytoplankton growth in the lake, which will lead to the lack of resources such as oxygen, and cause the death of other organisms [4,5]. Usually, the concentration of phosphate in water is very low (typically below 100 ppb). Many reviews have discussed the design and fabrication of phosphate sensors [4-7].

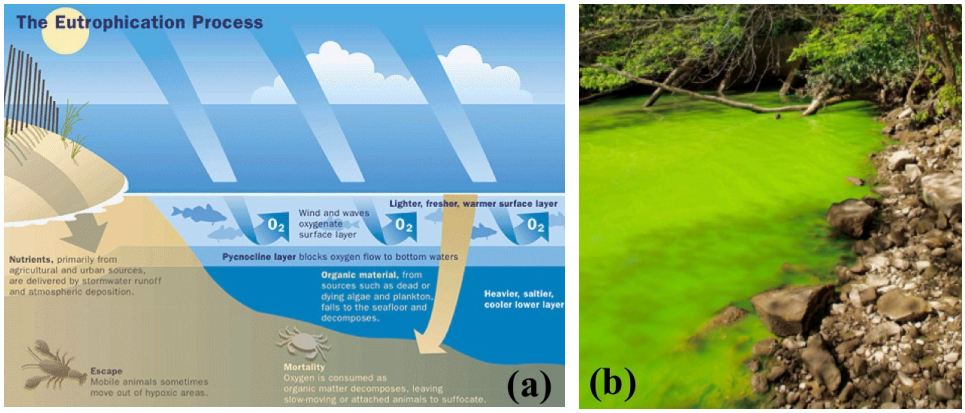

Figure 2. (a) the description of the eutrophication process; (b) the photo of the eutrophication of a lake

In general, many sensors or methods have been developed by research labs. Usually, these sensors will recognize the particular chemical first, then transfer it into a measurable physical signal. These physical signals include: mechanical transduction, optical transduction, electrochemical transduction and electric transduction.

Mechanical transduction can transfer the chemical reaction to a swelling strain [10] and detects mass changes. The mass change could be detected by the changes of resonance frequency (quartz crystal microbalance). The most common application of mechanical transduction is a quartz crystal microbalance (QCM), which is a very sensitive quality inspection instrument with an accuracy measured to nanograms. It can detect small amounts of the adsorb compound, and has been used in the water quality sensing applications.

There are many types of sensors based on the optical properties of absorbance, fluorescence, luminescence and light scattering. However, they cannot provide sufficient quantification. Colorimetry is the most common optical detection principle applied in sensing. It is easily read by eyes or with a common detector like a camera. However, it suffers from the disadvantage that the chemical reagents are required for the detection.

The electrochemical sensor works by reacting with the measured gas or liquid and producing an electrical signal proportional to the sample's concentration. Usually, this kind of sensor contains electrodes and electrolytes. Chemical reactions involve electric charges moving between electrodes and an electrolyte. Recently, a low cost, miniaturized and sensitive electrochemical based nitrate sensor was designed for remote quantitative determination of nitrate in ground water samples [11]. In the sensor [***Fig.3***], a concentric design for working- and counter-electrodes was used, to improve the uniformity of current distribution between electrodes. The working- and reference- electrodes were fabricated with sliver, and the counter electrode was fabricated by gold. The thickness of the electrodes is 200 nm.

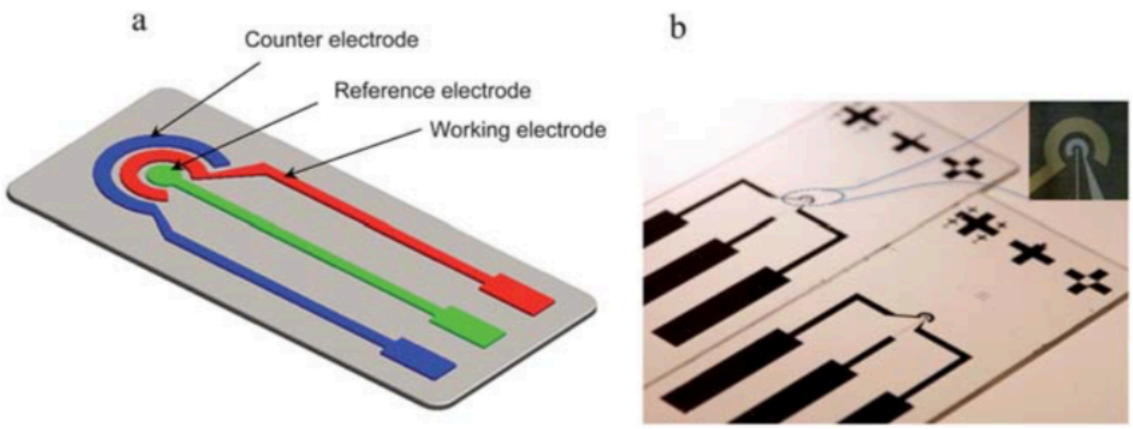

Figure 3. Microfabrication of the sensor. (a) Schematic of the three electrodes system of the nitrate microsensor. (b) Optical image of the microsensor

The nitrate reduction follows a two electrons transfer process to form nitrite:

$$NO_3^- + 2e + H_2O \rightarrow NO_2^- + 2OH^-$$

However, the electrochemical techniques suffer from the following disadvantages:

- Chemical erosion: Usually, some chemicals will be generated during the reaction. These chemicals will corrode the electrodes and decrease the sensor's lifetime.
- Specificity: Electrochemical sensors are susceptible to be interference from other gases in the air. In addition, detection of multiple chemicals in the sample at the same time is impossible, because all the chemical reactions convert concentrations to common outputs: currents and voltages.
- Temperature: The sensors are usually very sensitive to the temperature because it is easy to generate heat between electrodes.

Current widely-used techniques include UV spectrometry, ion chromatography, high-performance liquid chromatography and capillary electrophoresis. These conventional techniques are performed with bench-top equipment [12-13]. These techniques are unsuitable for on-site

operation in the field, and unaffordable for large-scale field deployment due to their cost, bulky size and complex measurement procedures. Other approaches for sensing nutrients in water are needed. One interesting technique uses microplasma and these devices have been used to detect metals in water samples [14]. Herein, a nutrient sensor based on fluidic microplasma technology is demonstrated.

Principle of the glowing microdischarge signal

The principles of the emission spectrum are illustrated in ***Fig.4***. Atoms or molecules at a high energy level generate radiation when they transition to lower energy levels. During this process, the excess energy will be emitted in the form of photon. The energy of the photon released equals the energy difference between the two levels. For each atom or molecule, there are many possible transitions, and each transition responds to an energy with a specific wavelength. Therefore, the emission spectrum of each element is unique. High voltages are used to move electrons from low energy levels to high energy levels. Based on this theory, spectroscopy has been used to identify the elements in unknown constituents.

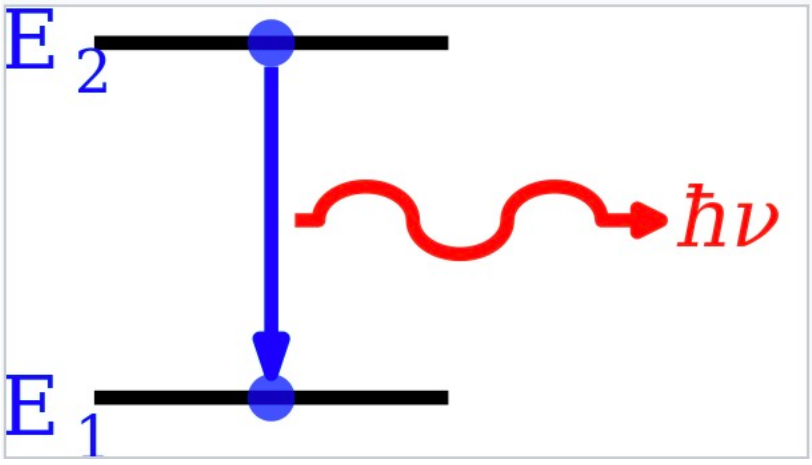

Figure 4. the principle of the emission spectrum

Device description and fabrication process

Device description

The sketch of the device and testing setup is shown in ***Fig. 5***. The microplasma device consists of two electrodes [14]. One metal electrode (cathode) is directly connected with the water sample, which is inside a water sample holder, serving as a water electrode. The other metal electrode is positioned very closely to the water sample. A DC voltage can be applied (~500 V) between the two electrodes [14-16]. In addition, the device has an Al-coated spherical surface (the radius and height of the spherical surface have been calculated) to ensure the light from the microplasma can be collected by the optical fiber probe efficiently, leading to a spectrometer.

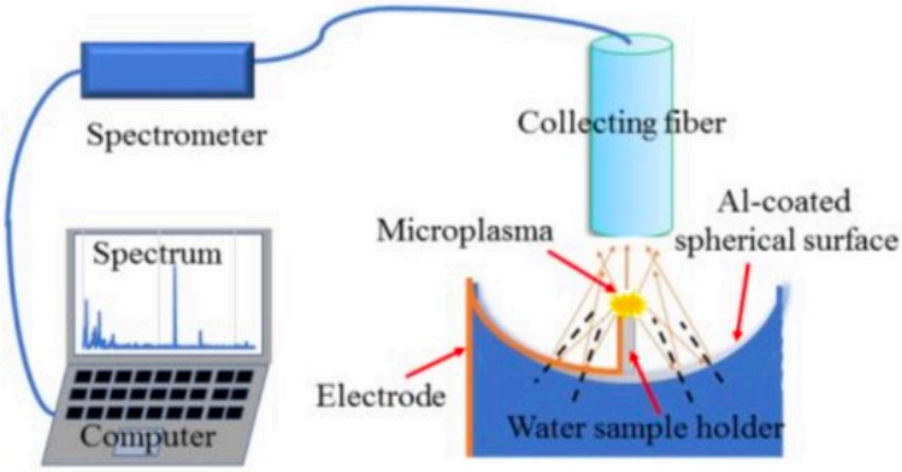

Figure 5. the setup for collecting the spectra of the water sample from the microplasma device: sketch of the microplasma device with an Al-coated spherical surface to enhance the collection of the optical signal

Device Fabrication

The device was fabricated using the process flow developed in our lab. The basic process flow is illustrated in ***Fig. 6***. First, we designed a spherical mold. The radius and the height of the

mold need to be calculated before because it decides the spherical surface on the device. Polydimethylsiloxane(PDMS) with a weight ratio 10:1 was used to cover the bottom of the mold, followed by 1.5 hours of curing at the temperature of 65 °C. Then a steel ball was chosen and put into the mold with liquid PDMS (weight ratio 10:1), followed by the same process of bake 1.5 hours at the temperature of 65 °C. Then, an aluminum layer (2-3 μm thick) was coated on the surface of the device by using E-beam evaporation. In the end, a small PDMS holder was designed and placed on the center of the device. This PDMS was used to hold the water sample and connect to electrodes (cathode). The optical fiber was placed vertically above this holder and the glowing microdischarge signal will be generated between the optical fiber and PDMS holder.

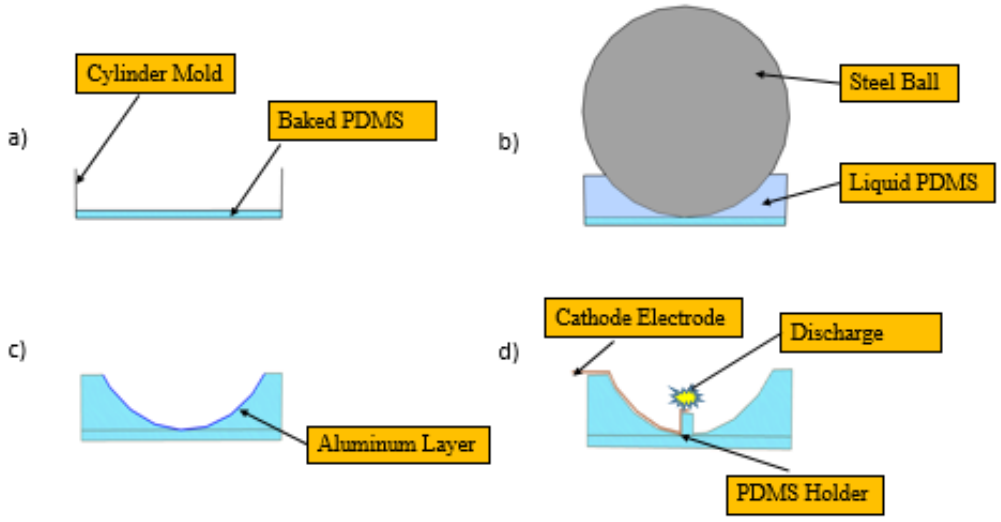

Figure 6. Fabrication process flow of the fluidic microplasma device

Result and discussion

A photo of a fabricated device is shown in ***Fig. 7***. Using the setup illustrated in ***Fig. 5***, the measured spectra using the new device and the device with a planar surface for Na_2HPO_4 water sample are shown in ***Fig. 8***. Clearly the new device can more efficiently capture the signals. To

demonstrate the detection of nitrate, we tested $NaNO_3$, KNO_3 and HNO_3 water samples. For the control experiments, NaCl water sample was tested. As shown in ***Fig. 9***, the characteristic spectra of nitrate can be clearly observed except for NaCl water sample. In addition, the major spectrum at 360 nm for N_2 can be routinely observed. This is because all the experiments have been performed in air ambient, thus the N_2 in air emits its characteristic spectrum from the microplasma.

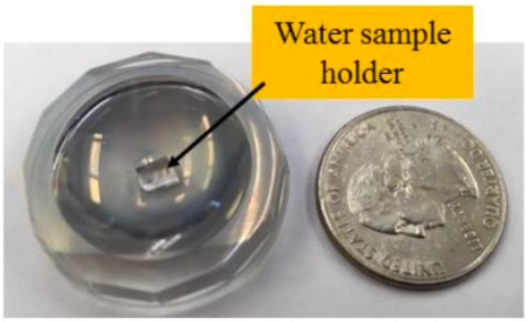

Figure 7. Photo of a fabricated device with a Quarter dollar

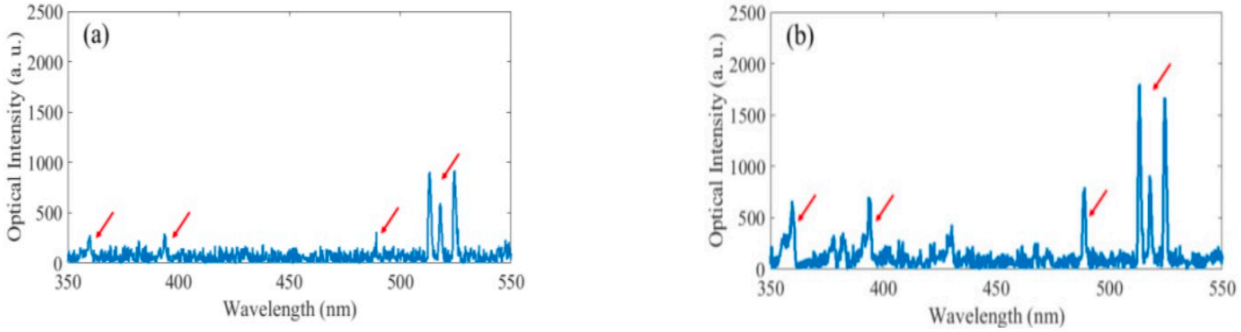

Figure 8. Optical signal collection from a microplasma device (a) with a planar surface and (b) with a spherical surface: the spectra pointed by red arrows clearly enhanced by the device with an Al-coated spherical surface.

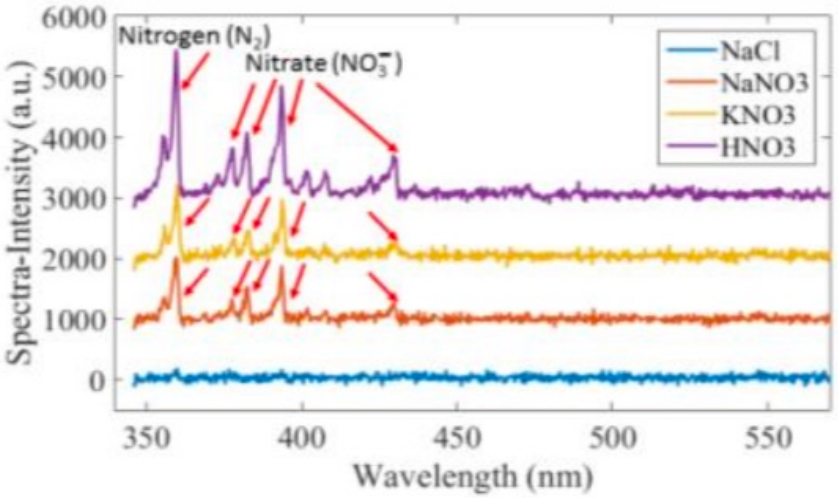

Figure 9. Measured emission spectra form NaCl (1 mol/L), NaNO3 (1 mol/L), KNO3 (1 mol/L), and HNO3 (5%) water samples in air with lines separated intentionally by 1000 along the y axis for clearer visibility.

The multiplexed detection capability of the devices has also been demonstrated. Specifically, we tested a mixed water sample of Na_2HPO_4 and $NaNO_3$, and the characteristic spectra for both nitrate and phosphate are clearly observed as shown in ***Fig. 10***.

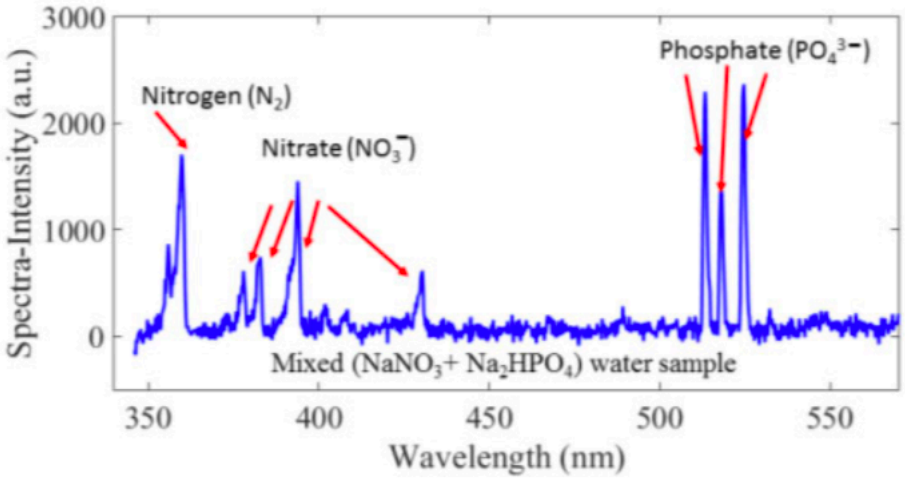

Figure 10. Measured emission spectra from a mixture of Na2HPO4 (1mol/L) and NaNO3 (1 mol/L).

It has been observed that the spectral intensities of the nitrate increase with their

concentrations. Hence some experiments to demonstrate the possibility to determine the concentration of nitrate in water have been carried out. In this case, the intensity of the nitrogen (N_2) spectrum at 360 nm (assume N_2 concentration is constant in the air ambient), which are seen in all microdischarge, is used as a reference [14]. For example, by measuring the ratio of the spectra intensities of the primary nitrate (393 nm) to N_2 (360 nm), it is possible to determine the concentration of the nitrate over a wide dynamic range (10 ppm to 1500ppm) as shown in ***Fig. 11***.

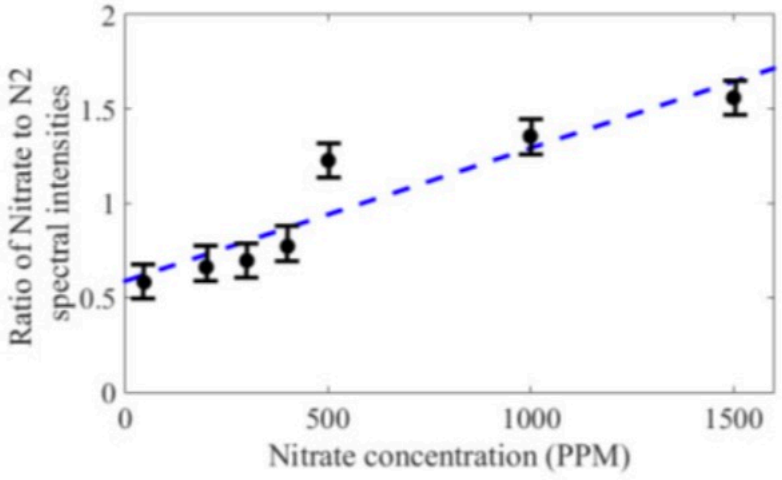

Figure 11. Ratio of nitrate to N2 spectral intensities as a function of nitrate concentration

Conclusion and future work

The detection of nutrients including nitrate and phosphate in water using a fluidic microplasma chip with an Al-coated spherical surface has been demonstrated. This chip is possible to detect concentration of the nutrients in water. However, a datasheet related to the specific nutrient concentration (ratio of nutrients in water to N_2 spectral intensities vs nutrients concentration) need to be made in the future. Drinking water, water from lake and streams and water from ocean need to be tested to confirm the influence of impurities on the signals that the device is able to detect. The performance of our device is compared to other technologies in the

following table:

Techniques	Operation	Cost	specificity	Detection limit	Multiplex detection
HPLC	Complex	Expensive	Excellent	Excellent	Multiple
UV spectrometry	Complex	Expensive	Excellent	Excellent	Multiple
Electrochemical sensor [13]	Easy	Cheap	Good	Excellent	Single
The fluidic microplasma sensor	Easy	Cheap	Excellent	Good	Multiple

Acknowledgements

Research supported by Exploratory Research Program from College of Engineering at Iowa State University.

References

[1] Moorcroft M J, Davis J and Compton R G 2001 Detection and determination of nitrate and nitrite: a review *Talanta* 54 785–803

[2] Miro M, Estela J M and Cerda V 2003 Application of flowing stream techniques to water analysis. Part I. Ionic species: dissolved inorganic carbon, nutrients and related compounds *Talanta* 60 867–86

[3] Bühlmann P, Pretsch E and Bakker E 1998 Carrier-based ion-selective electrodes and bulk optodes. 2. Ionophores for potentiometric and optical sensors *Chem. Rev.* 98 1593–688

[4] Stoddard J L, Van Sickle J, Herlihy A T, Brahney J, Paulsen S, Peck D V, Mitchell R and Pollard A I 2016 Continental-scale increase in lake and stream phosphorous: are oligotrophic systems disappearing in the United States? *Environ. Sci. Technol.* 50 3409 – 15

[5] Maavara T, Parsons C T, Ridenour C, Stojanovic S, Dürr H H, Powley H R and Van Capellen P 2015 Global phosphorous retention by river damming *Proc. Natl Acad. Sci.* 112 15603 – 8

[6] Berchmans S, Issa T B and Singh P 2012 Determination of inorganic phosphate by electroanalytical methods: a review *Anal. Chim. Acta* **729** 7 – 20

[7] Warwick C, Guerreiro A and Soares A 2013 Sensing and analysis of soluble phosphates in environmental samples: a review *Biosens. Bioelectron.* **41** 1 – 11

[8] Estela J M and Cerda V 2005 Flow analysis techniques for phosphorous: an overview *Talanta* **66** 307 – 31

[9] Hsu L H H and Selvaganapathy P R 2014 Stable and reusable electrochemical sensor for continuous monitoring of phosphate in water *IEEE Sensors* **14** 1423 – 6

[10] Godin M, Tabard-Cossa V, Grütter P and Williams P 2001 Quantitative surface stress measurements using a microcantilever *Appl. Phys. Lett.* 79 551 – 3

[11] Gartia, Manas Ranjan, et al. "The Microelectronic Wireless Nitrate Sensor Network for Environmental Water Monitoring." *Journal of Environmental Monitoring, vol. 14, no. 12, 2012, p. 3068*

[12] P. Rundel, E. Graham, M. Allen, J. Fisher, T. Harmon, "Environmental sensor networks in ecological research," *New Phytologist*, 182(3), 589-607, 2009.

[13] M. R. Gartia, B. Braunschweig, et al, "The microelectronic wireless nitrate sensor network for environmental water monitoring," *Journal of Environmental Monitoring*, 14(12), 3068-3075, 2012.

[14] C. Wilson and Y. B. Gianchandani, "Spectral detection of metal contaminants in water using an on-chip micro- glow discharge," *IEEE Transactions on Electron Devices*, 49(12), 2317-2322, 2002.

[15] L. Que, C. Wilson, Y. B. Gianchandani. "Microfluidic electrodischarge devices with integrated dispersion optics for spectral analysis of water impurities." *Journal of microelectromechanical systems*, 14(2), 185-191, 2005.

[16] B. Mitra, C. Wilson, L. Que, P. Selvaganapathy, Y. B. Gianchandani. "Microfluidic discharge-based optical sources for detection of biochemicals." *Lab on a Chip*, 6(1), 60-65, 2006.

APPENDIX A. STUDIES OF CELL BEHAVIORS IN 3D MICROTISSUES IN A MICROFLUIDIC DEVICE: GROWTH AND MIGRATION

Modified from a paper submitted to IEEE-Sensors and a paper submitted to micromachines

Xiangchen Che, Jacob Nuhn, Shenmin Gong, Ian Schneider, Long Que

Abstract

This paper reports, an optimized microfluidic droplet device for fabricating 3D microtissues and studying the cell behaviors in 3D microtissues. It has been found by properly selecting the size of the microchambers on the microfluidic device and choosing an optimal concentration of collagen (2 mg/ml) to fabricate microtissues, the behaviors of cells in the microtissues can be essentially the same as those of cells in a conventional cell culture system. The normal cell spreading and division in the microtissues have been observed, and the cell migration speed is ~14.1μm/hr, close to that of 16.2 μm/hr in a macroscale tissue. All these experimental results suggest the microfluidic droplet device might provide a new avenue to replace other approaches to fabricate 3D microtissues and study cell behaviors.

Introduction

Traditional cell culture system, which can only offer 2 dimensional (2D) tissues and cannot isolate single cells or groups of cells, is difficult to be used as technical platform to uncover how cells respond to the extracellular matrix (ECM) and how cells communicate [1-2].

The platform has the following features: (a) the platform can realize the encapsulation of

cells in ECM similar to that in human body. The ECM should be 3 dimensional. (b) the platform can achieve the isolation of single cells or groups of cells in order to control the cell-cell communication. (c) the platform allows to build microenvironments that are sufficiently small such as microtissues. (d) the platform can rapidly generate a large number of cell-encapsulated microtissues in parallel in a cost-effective manner for high throughput studies.

The microfluidic device we developed and used to fabricate 3D microtissues and study the cell migration in this paper coined as *first-generation* device [8]. However, it was found that the cell migration speed inside microtissue, which has a volume of ~600 pL, is ~ 2 μm/hr lower than that of the same type of cells when they are in macroscale tissue of 16.2 μm/hr [3]. Fuethermore, due to the size/volume limitation of the microtissue, the proper growth of the cells cannot be observed. Basically, at this volume size range, the behaviors of cells are different from those of cells when they are at a large-scale tissue environment.

In order to study the cells' behaviors in microfluidic devices with the aforementioned features, meanwhile in order to ensure their behaviors are essentially the same as those in the large-scale environment, in this effort, we modify the dimensions of the microfluidic device (coined as *second-generation* device) and evaluate the cells' behaviors for the first time.

Description of the microfluidic device

The droplet microfluidic device for generating arrayed microtissues is given in ***Fig. 12***. Filtered silicone oil is used as the continuous flow phase and the carrier fluid. Along the flowing direction of the fluids as illustrated in ***Fig. 12***, this device consists of a T-shape droplet generator, a liquid-droplet merger, a serpentine control-channel (c-channel), and the droplet storage-chambers (chambers). The droplet generator forms cell-laden collagen droplets. The c-channel is

designed to prevent any air bubbles or non-uniform droplets from entering and occupying the chambers at the beginning of the operation of the device [3]. Once the uniform droplet generation is established, the c-channel is closed, and the outlet of the chambers is open. As a result, the droplets will flow toward the chambers, thereby entering and occupying them one by one. Compared to the *first-generation device* [3], the dimensions of the *second-generation devices* have been scaled up. Specifically, the diameter of the chamber increases from 120 μm to 360 μm, while the width of the flowing channel increases from 50 μm to 150 μm. The height of the chamber has been designed as 30 μm and 80 μm, respectively for two types of the second-generation devices.

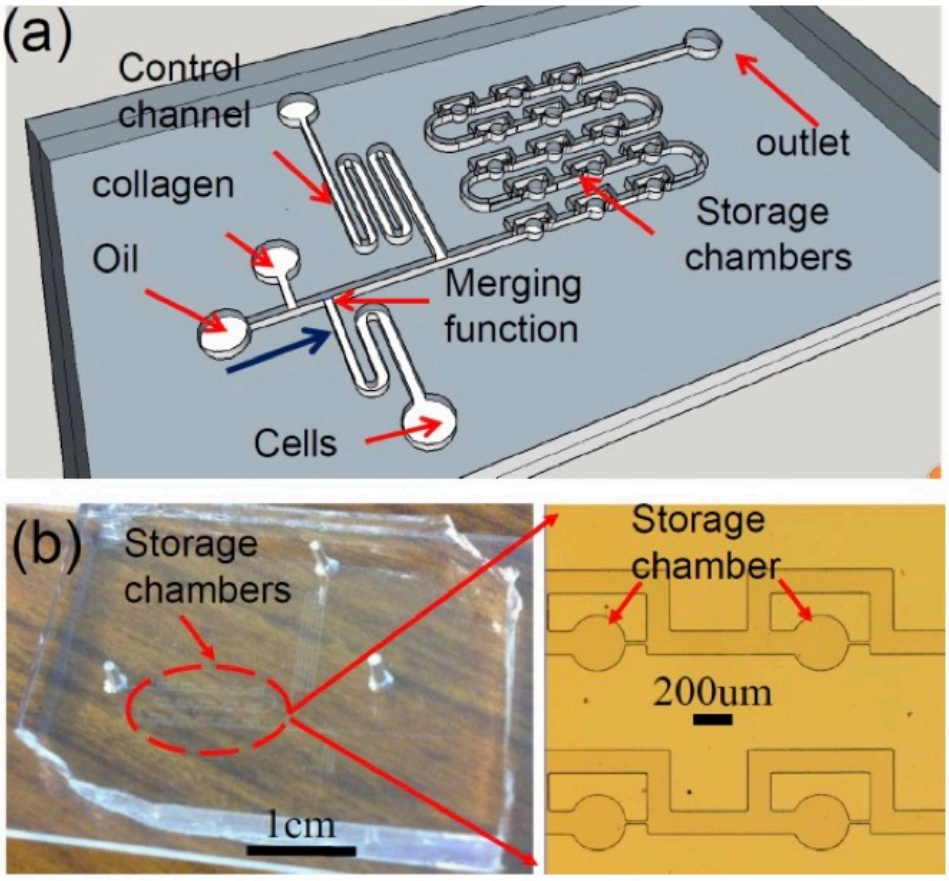

Figure 12. (a) Sketch of the droplet microfluidic device for generating 3D microtissues: Each storage chamber (a cylinder with a radius of 180 μm and height of 30 or 80 μm) has one 3D microtissue containing single or multiple cells; (b) photo of a fabricated chip with 15 storage chambers; (c) optical micrography showing the storage chambers

Device fabrication and experimental procedure

Device fabrication

The device is fabricated using a soft lithography process. Briefly, a SU-8 mold (30 μm, 50 μm and 80 μm thick) of the device is formed on a silicon substrate. Polydimethylsiloxane (PDMS) is then casted on the mold, followed by 1.5 h of curing at the temperature of 65 °C. Finally, the PDMS microfluidic layer is peeled off from the mold, and then bonded with a glass substrate after oxygen plasma treatment for 10 seconds. The input and output holes are made in the PDMS layer for the delivery of the samples to the chip, followed by assembling input and output tubing (Upchurch Scientific, Inc., Oak Harbor, DC, USA)

3D microtissues fabrication procedure

The device is firstly soaked in PBS buffer solution (pH –7.4) in incubator (FISHER SCIENTIFIC-ISOTEMP 3530) overnight [3]. Silicone oil (SIGMA-ALDRICH) is used as the fluid carrier. The cell loading in the collagen droplets is based on Poisson distribution during the experiments. No surfactant is used to facilitate the droplet stability. The collagen flowing input tube and syringe and submerged into a cold-water tank (0~2 °C) to avoid fast polymerization. After the droplets are in the chambers, the device is flipped over regular until the collagen is fully polymerized, thereby making sure the cells are in the middle of the storage chamber (along z-axis), namely the cells in the 3D-matrix.

Materials and methods

Breast cancer MDA-MB-231 cells were subcultured in Dulbecco's modified Eagle's medium with 10% fetal bovine serum, 2% Glutamax, and 1% penicillin/streptomycin. Imaging media was the same except it lacked phenol red and was supplemented with 12 mM HEPES. On the day the chambers were loaded, cells were trypsinized and suspended in 2 mg/mL collagen

solution (rat tail-CORNING-354249) neutralized with imaging media at a cell density of 2×10^6 cells/mL. Chips were either loaded with a continuous collagen phase or with droplets in the storage chambers. Cells were allowed to spread over 24 h. Phase contrast images were then taken every 0.5–2 min over 4–8 h. Slabs of collagen were generated between two microscope slides with 60 μm (thin) or 360 μm (thick) spacers. Cells were prepared and imaged in the same way as for the devices with the exception that 3×10^5 cells/mL were used.

In order to mitigate or even eliminate the droplet shrinking issue due to evaporation, the fabricated chip was firstly soaked in PBS buffer solution (pH-7.4) in incubator (FISHER SCIENTIFIC-ISOTEMP 3530) overnight before use to ensure that PDMS was saturated with PBS. Silicone oil (SIGMA-ALDRICH) was used as the fluid carrier. Harvard syringe pump (70–4500) was connected with syringes for flowing the oil and the collagen/cells. In the experiments, the cell loading in the collagen droplets was based on Poisson distribution without any attempt to control the loading process. In addition, no surfactant was used to facilitate the droplet stability. During the collagen droplet generation and storage process, the collagen flowing input tube and syringe were submerged into a cold water tank (0~2 °C) to avoid fast polymerization since the polymerization rate is highly depended on temperature. After the droplets were stored in the chambers, the device was flipped over every minute within 10 min until the collagen was fully polymerized in the storage chamber, and to make sure the cells were in the middle of the storage chamber (along the *z*-axis), thereby ensuring the cells to stay in the 3D-matrix. For the experiments, the droplet microtissues remain surrounded by silicone oil. Experiments on the cell behaviors after the oil is replaced by cell culture media are in progress.

Confocal reflectance microscope (LEICA LAS-AF, Weltzlar, Germany) was used to image the 3D-matrix system. Standard incubator (FISHER SCINTIFIC-ISOTEMP 3530, FISHER

SCINTIFIC, Waltham, MA, USA) was used to incubate the chip overnight in order to make cells accommodate to 3D-matrix system for cells' optimum behavior. OLYMPUS IX73 (OLYMPUS, Tokyo, Japan) with camera DP73 (OLYMPUS, Tokyo, Japan) was used to track the cell migration.

During the cell tracking process, the chip was submerged into a glass petri dish filled with PBS buffer at 37 °C to prevent drying problem. A heating stage (HARVARD APPARATUS-c-11842, HARVARD APPARATUS, Holliston, MA, USA) was applied to supply continuous heat. Finally, image J (National Institutes of Health, Bethesda, MD, USA) with a cell tracker model was used to track and plot the cell migration diagram. Experiments found that oxygen depletion was not a problem, even in our relatively small microtissues with PDMS and media above. Cell death did not occur over the period of about two days in the chamber, particularly if it was kept under proper pH buffering and temperature conditions. The oxygen consumption rate (OCR) for cancer cells is no higher than 30 $\text{pmol}\cdot\text{s}^{-1}\cdot10^{-6}\cdot\text{cells}$ [3]. The volume of each microtissue is ~6.0×10^{-10} L and no more than 10 cells occupy a microtissue. Consequently, the OCR for one microtissue is 500 nM/s. If no oxygen transfer occurs, it would take over a day for the cells in each microtissue to decrease the oxygen concentration from 260 μM, the saturated level of media in equilibrium with air in the incubator, to 200 μM, a value still well above hypoxic conditions. However, there is oxygen transport across the liquid and PDMS, and the transport is governed by the following equation at steady state: $\text{OCR} = (D/h)A(C^* - C)$, where OCR is the oxygen consumption rate (0.3 fmol/s), D is the diffusion coefficient of oxygen in PDMS or water (3×10^{-5} cm^2/s) [4], A is the cross-sectional area of each microtissue (1.2×10^{-4} cm^2), C^* is the equilibrium concentration of oxygen in fluid (260 μM), C is the local oxygen concentration around the cells and h is the height of the PDMS and fluid above the microtissue. At a height of 0.8 cm, the steady-state oxygen concentration is about 200 μM. While there is little information on whether cell function is altered

at this concentration, it is well above that which is considered hypoxic (<6 μM). Furthermore, because media is initially at an equilibrium concentration of 260 μM oxygen, it takes time for the oxygen concentration to reach this steady state. At the time that experiments are conducted, the oxygen level is 200–210 μM. Consequently, the 0.8 cm of PDMS and media is thin enough to support the relatively low rate of oxygen consumption within the microtissues.

Results and discussion

Droplet capture

The optical image of the fabricated arrayed microtissues inside the storage chambers is given in ***Fig 13*** The optical image of the fabricated arrayed microtissues inside the storage chambers is given in ***Fig 13a***. Following the procedure described in Section 2, it has been demonstrated that the uniform microtissues can be formed and stored in the storage chambers on the chip routinely. However, it should be emphasized that care should be taken to avoid the polymerization of the collagen in the flowing channels on the chip; otherwise, the storage chambers cannot be occupied by microtissues properly. In ***Fig 13b***, a close-up optical image of a droplet shows a cell inside a polymerized collagen fiber. In order to show the collagen fiber more clearly, a confocal image in ***Fig 13c*** has been taken on the droplet, showing one cell embedded in the polymerized collagen fiber.

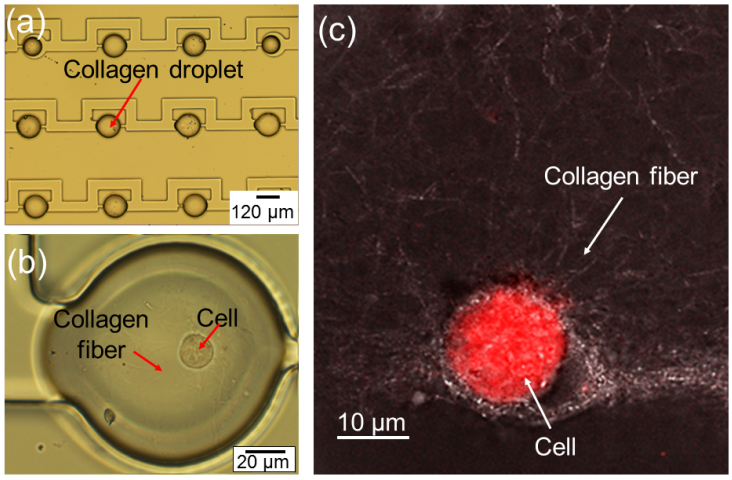

Figure 13. (a) Photo of arrayed microtissue stored in storage chambers; (b) close-up of one microtissue containing one cell; (c) confocal image of one cell inside polymerized collagen fiber, forming a microtissue

Droplet environment

In order to confirm that the cell is indeed surrounded by a 3D extracellular matrix (ECM), which is made up of polymerized collagens, some confocal images of the microtissues have been taken. A topside view, cross-section view and the stacked images from the bottom to the top of a microtissue are obtained in ***Fig 14***. Given that the nominal height of the fabricated storage chambers is ~50 µm, the cell is roughly ~20 µm above the bottom of the microtissue and ~20 µm below the top of the microtissue. Basically, the cell is embedded inside the collagen fibers. Note that the gap of the cell from the top and bottom of the microtissue can be readily increased by increasing the height of the storage chambers.

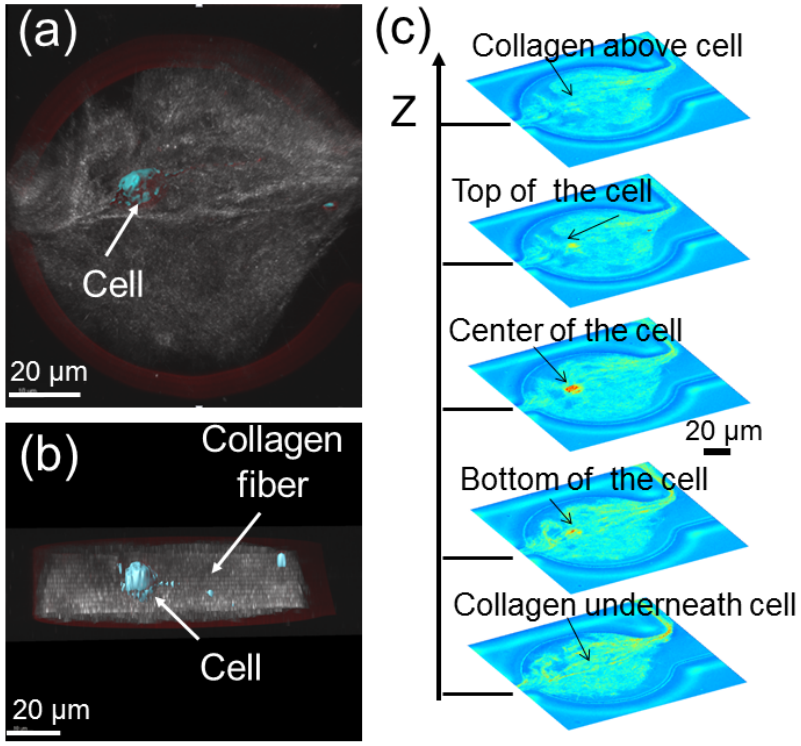

Figure 14. Confocal images showing one cell inside a 3D microtissue in a storage chamber: (a) topside view; (b) cross-section view; (c) stacked confocal images of a microtissue showing one cell inside a 3D microtissue

It has been found that as long as the silicone oil does not directly contact the cells, it will not affect cell viability. In the experiments, only the cells embedded within the polymerized collagen have been studied. These cells are not directly exposed to oil. The total time for the cells inside the polymerized collagen for the experiments was up to 32 h, and no clear effect on cell viability was observed during this time period, suggesting that the oil does not diffuse into the microtissue droplets.

It has also been observed that the polymer gel structure has some differences at the interior *versus* the edges of the microtissue droplets. Interactions with surfaces could potentially nucleate collagen fiber assembly or simply act as an adherent surface for collagen fibers. The typical time

for the polymerization of the collagen is ~15 min at room temperature, similar to that for collagen polymerization on a glass cover slip.

The real-time migration videos (in the supplementary) of the cells inside microtissue have been recorded using an optical microscope. The representative images in ***Fig 15, (a) and (b)*** shows the migration of three congregated cells inside microtissue in a 7 h period of time, while the representative images in ***Fig 15, (c) and (d)*** shows the migration of one cell inside a microtissue during the same period of time. These experiments demonstrate that the chip can provide a platform to study the migration of one single cell or multiple cells in a microtissue environment. In addition, since the cells are confined in a small volume (~600 pL), the communication among them may be easily studied.

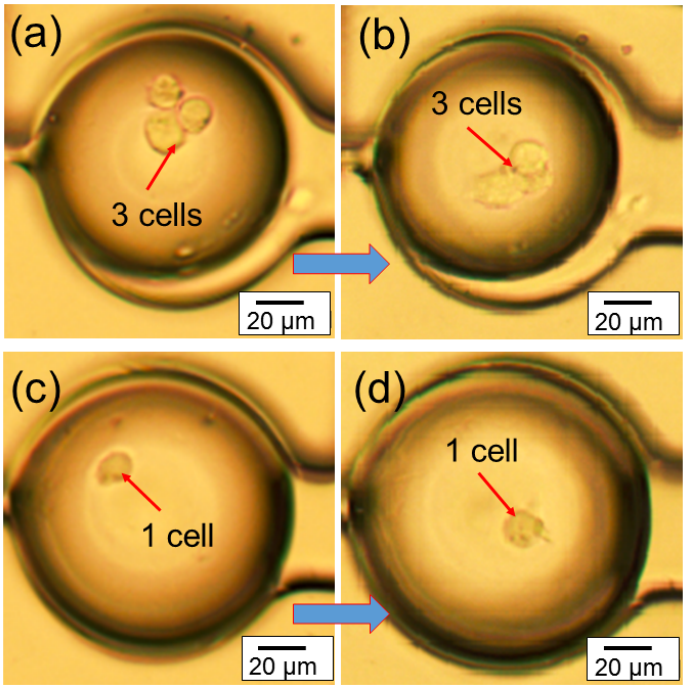

Figure 15. Representative optical images showing (a,b) the migration of three cells inside 3D microtissue during a 7 h period at 37 ° C; (c,d) the migration of one cell inside 3D microtissue during a 7 h period at 37 ° C.

Results of the first-generation device

Based on the recorded videos (in the supplementary), the cell migration speed has been calculated under two conditions. The first condition includes chips that are filled with cells embedded in collagen, generating a continuous collagen network. This increases the volume of the environment, decreasing the opportunity for the depletion of nutrients or accumulation of waste. Also, cells in different chambers may communicate. The second condition includes devices that only contain cells embedded in collagen in droplets within the chambers (***Fig 15***). These droplets have relatively small volumes and cells in a particular droplet cannot communicate with cells in other droplets. These conditions were compared to cell migration in thin (60 μm) and thick (360 μm) slabs of collagen. Representative migration trajectories are shown in ***Fig 16 (a) and (b)***. Cells in the continuous collagen gels migrate similarly to those in the thin collagen slabs and slower than those in the thick collagen slabs (***Fig 16c***). Cells in droplets migrated much slower than any other condition (***Fig 16c***).

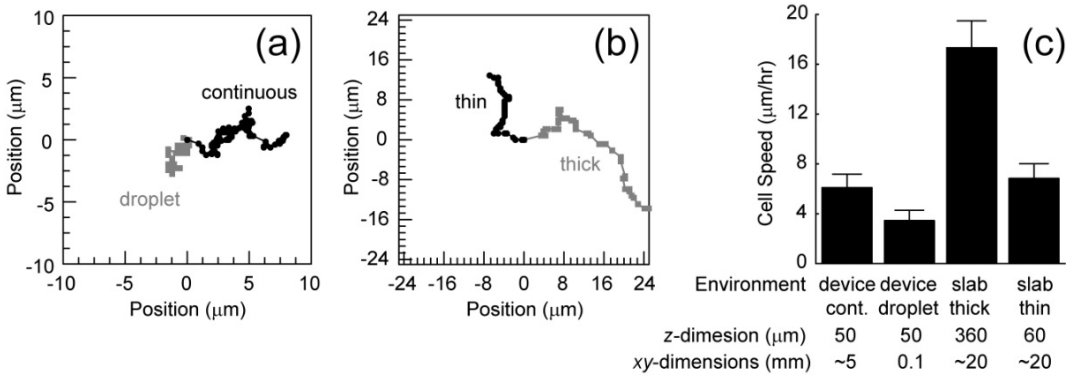

Figure 16. Representative trajectories of cells embedded in collagen (2 mg/mL) in the chip (a) and embedded in a collagen (2 mg/mL) slab between two coverslips (thick: grey, thin: black); (b) The chip is either filled with a continuous polymerized collagen network (grey) or droplet of collagen within the chambers (black); (c) Average cell speed under the different conditions as well as the length scales associated with each condition. Error bars are 95% confidence intervals.

It is interesting that the chip filled with a continuous collagen network and a thin slab results in similar migration rates. Collagen stiffness is known to alter migration speeds and the observed stiffness of flexible networks changes close to stiff interfaces, a so-called wall effect. The similar *z*-dimension length scales between these conditions likely generate the similar migration speeds. Consequently, thicker polymerized collagen networks in the chips are likely needed to observe faster migration. Finally, the droplet *xy*-dimensions length scales are much smaller than the other conditions suggesting that either (1) cells require communication between chambers or (2) small volumes in this first-generation chip inhibit migration. The second-generation chips with storage chambers that are both thicker and larger will allow us to eliminate the wall effects and focus on cell-cell communication within and between chambers that governs cell migration.

Cell spreading in 3D microtissue (the second-generation device)

Representative images showing the measured cell spreading in first generation device and the second-generation device are given in ***Fig 17***. As seen clearly, the cells are still alive but do not show apparent spreading after 24-hour incubation in the first-generation device. Basically, the shape of the cell remains roughly round 24 hours later. In contrast, the spreading of cells in the second generation is very obvious. The morphologies of the cells become essentially the same as those of cells grown inside the large-scale tissue in a conventional cell culture system, indicating as far as the dimensions are selected properly, the microtissue can provide similar biological environment for cells to that of macroscale tissue. The volume of the microtissue in the second-generation device is ~8140 pL in comparison with the volume of ~600 pL for the first-generation device.

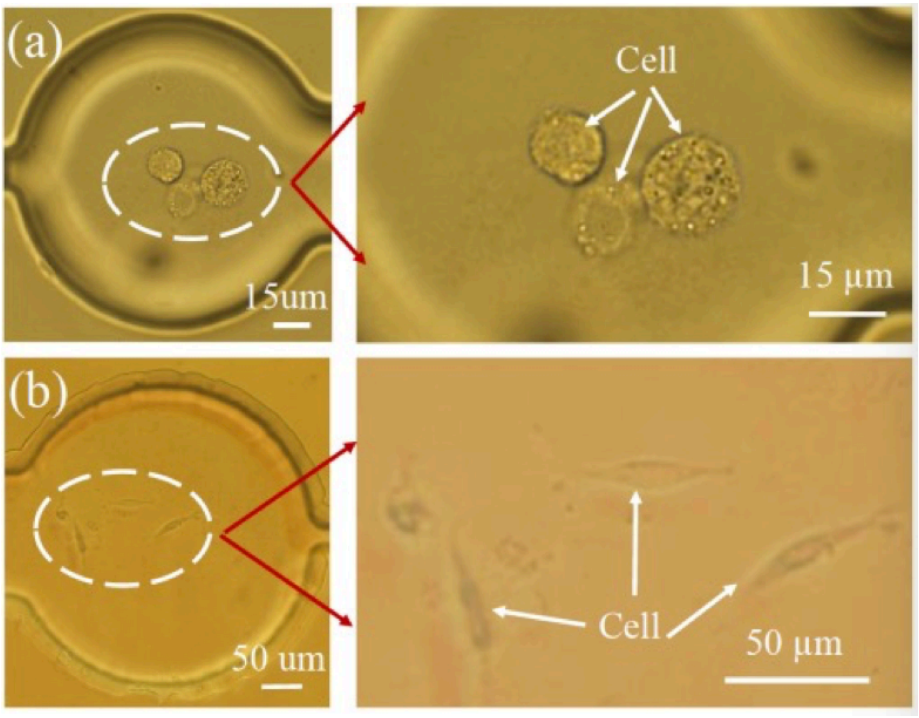

Figure 17. Cell spreading in 3D matrix within (a) small chamber of ~600 pL; (b) larger chamber of ~8140 pL volume after 24-hour incubation.

Cell division in 3D microtissue

Another important observation of the second-generation device is the cell division procedure as shown in ***Fig. 18***. In the first-generation device, the cell division was not observed, suggesting the size limitation of the tissue, resulting in the abnormal growth of the cells [8]. As shown clearly in the second-generation device, the cell becomes round shape in ***Fig. 18c***. then cell division occurs in ***Fig. 18d***. after the two daughter cells are formed in ***Fig. 18c***, they grow normally in ***Fig. 18f***.

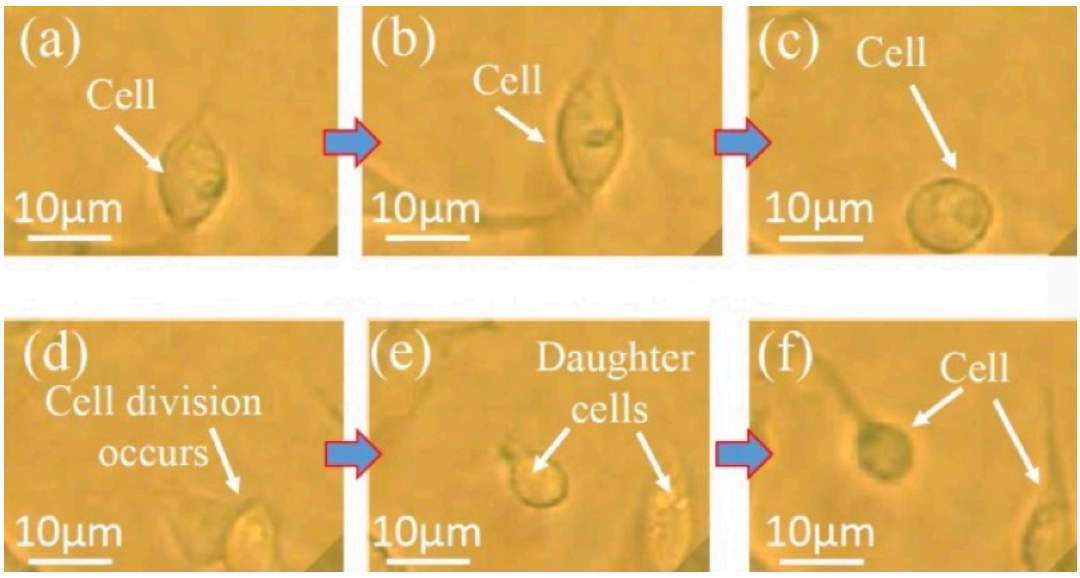

Figure 18. Optical micrographs showing the cell spreading and growth procedure in a 3D microtissue

Cell migration trajectory and speed in 3D microtissue

The videos of cells' migration inside microtissue have been recorded using an optical microscope [9]. Representative migration trajectories are given in ***Fig. 19a***. Compared to those in first generation devices, the range of the migration of cells has been significantly increased. For instance, the cell migration is within an area of 3 μm * 14 μm for the second-generation device. Also, the cell migration speed has been calculated based on the videos as shown in ***Fig. 19b***.

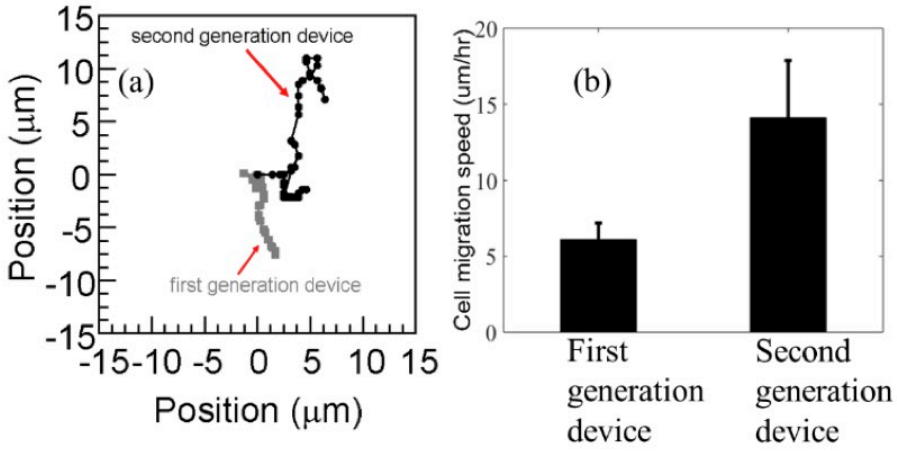

Figure 19. Comparison: cell migration trajectory (a) and migration speed (b) inside the microtissue fabricated in the first-generation device and the second generation.

Collagen concentration (tissue fiber density) effect on cell migration speed: Different concentration of collagen have been used to fabricate microtissues, resulting in microtissues with different densities. The measured cell migration speeds are summarized in ***Fig. 20***. It has been found that the lower collagen densities (1 mg/ml and 2 mg/ml) show an improved cellular migration speed over the higher collagen densities (3 mg/ml). This is due to the thick gel having more fibers to restrict the pore size within the matrix. An increased density of fibers would require more MMP activity to increase pore size and allow for higher freedom of movement. Note that collagen fibers must be dense enough for the cell to grow on, but not too dense to limit the cell migration speed. Experiments have found that 2 mg/ml is an optimal concentration for collagen because most of cell spreading and division are only observed at this value.

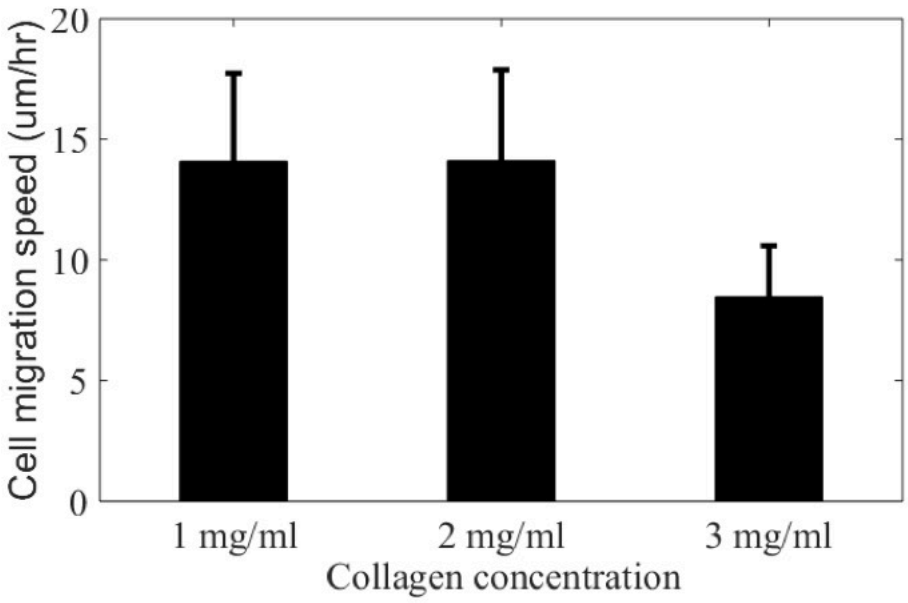

Figure 20. Collagen concentration (tissue fiver density) effort on cell migration speed. 2 mg/ml used as a standard concentration since most of cell spreading occurs and cell division is only observed at this concentration

Microtissue thickness (volume) effect on cell migration speed: In order to understand the cell speed influenced by the microtissue thickness (i.e. volume), devices with chamber thickness of 30 μm and 80 μm are fabricated, while the chamber diameter remains 360 μm for both types of devices. As shown in ***Fig. 21***, the average cell migration speed in 30 μm thick microtissue is ~7.1 μm/hr, which is much lower than that in 80 μm thick microtissue of 14.1 μm/hr. This indicates the microtissue thickness (volume) indeed affects the cells' behavior. For comparison, the measured cell migration speed in a slab of 360 μm thick tissue is ~16.2 μm/hr, very closed to the device with 80 μm thick microtissue.

For the device with an increased chamber height, and thus increased volume of microtissue, the cells migrate faster as a result of experiencing less edge effects, cellular waste taking longer to accumulate, and oxygen depletion within the gel requiring more time to affect the cells.

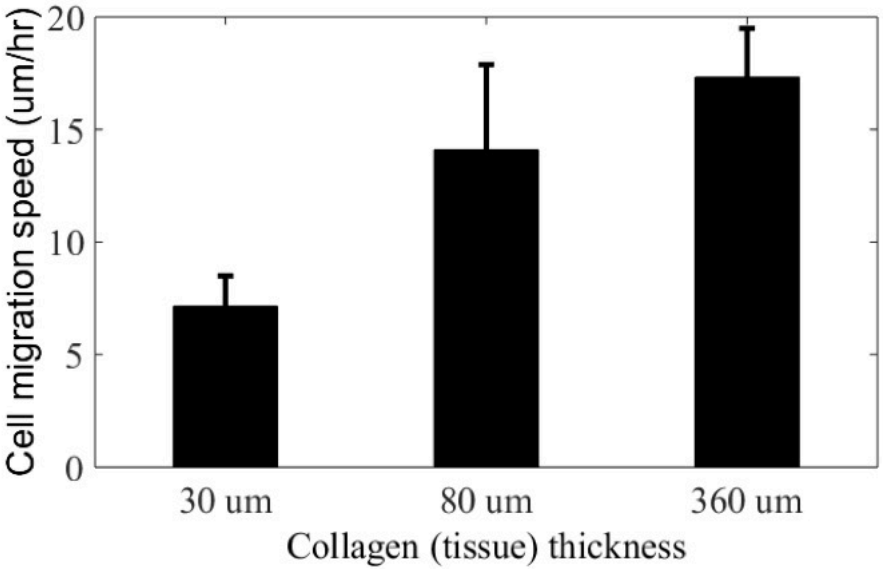

Figure 21. Thickness (volume) effect on the migration speed: the second-generation devices with chamber heights of 30 um and 80 um. A large gel with a height of 360 um. The cell migration speed in 30 um thick microtissue is half of that in 80 um thick microtissue, which is close to the migration speed in the 360μm thick tissue

These experiments indicate by adjusting the dimensions of our microfluidic device, the cells' behaviors in microtissue in a microfluidic device can be similar to that in the tissue fabricated in a conventional cell culture system. But the microfluidic device offers many advantages over the conventional cell culture system as mentioned in the Introduction section.

Conclusions

In summary, in this effort, we have demonstrated the possibility to use microfluidic devices to fabricate microtissues of *proper* sizes/volumes for studying the *normal* cells' behaviors including growth and migration, which are similar to those of cells in a large scale tissue. This technical platform opens a new avenue to study the behaviors of single cell and/or a group of cells in a in vivo – mimicking 3D microtissue environment.

References

[1] F. Pampaloni, G. Emmanuel, H. Ernst, "The third dimension bridges the gap between cell culture and live tissue." Nature reviews Molecular cell biology, vol. 8, no. 10, pp. 839-845. 2007.

[2] C. Fischbach, et al. "Engineering tumors with 3D scaffolds." Nature methods, vol. 4, no. 10, pp. 855-860, 2007.

[3] X. Che, J. Nuhn, I. Schneider, and L. Que. "High throughput studies of cell migration in 3D microtissues fabricated by a droplet microfluidic chip." Micromachines, vol. 7, no. 5, pp: 84, 2016

[4] Teh, S. S.-Y.; Lin, R.; Hung, L.-H.; Lee, A.P. Droplet microfluidics. *Lab Chip* **2008**, *8*, 198 – 220.

[5] Li, C.Y.; Wood, D.K.; Huang, J.H.; Bhatia, S.N. Flow-based pipeline for systematic modulation and analysis of 3D tumor microenvironments. *Lab Chip* **2013**, *13*, 1969 – 1978.

[6] Hong, S.M.; Hsu, H.J.; Kaunas, R.; Kameoka, J. Collagen microsphere production on a chip. *Lab Chip* **2012**, *12*, 3277 – 3280.

[7] Cheng, W.; He, Y.; Chang, A.; Que, L. A microfluidic chip for controlled release of drugs from microcapsules. *Biomicrofluidics* **2013**, *7*, 064102.

[8] Herst, P.M.; Berridge, M.V. Cell surface oxygen consumption: a major contributor to cellular oxygen consumption in glycolytic cancer cell lines. *Biochim. Biophys. Acta. Bioenerg*. **2007**, *1767*, 170 – 177.

[9] Cox, M.E.; Dunn, B. Oxygen diffusion in poly(dimethyl siloxane) using fluorescence quenching. I. Measurement technique and analysis. *J. Polym. Sci. Part A Polym. Chem.* **1986**, *24*, 621 – 636.

APPENDIX B. MASK SCHEMATICS AND DESIGN FUNCTION

The Appendix B shows the schematic masks and design functions for the microfluidic device.

The schematic of mask is showed in ***Fig. 22***. There are five patterns in the mask, which means can fabricate 5 devices once by using this mask. There are 15 chambers, 3 inputs channel, one control channel and one output channel.

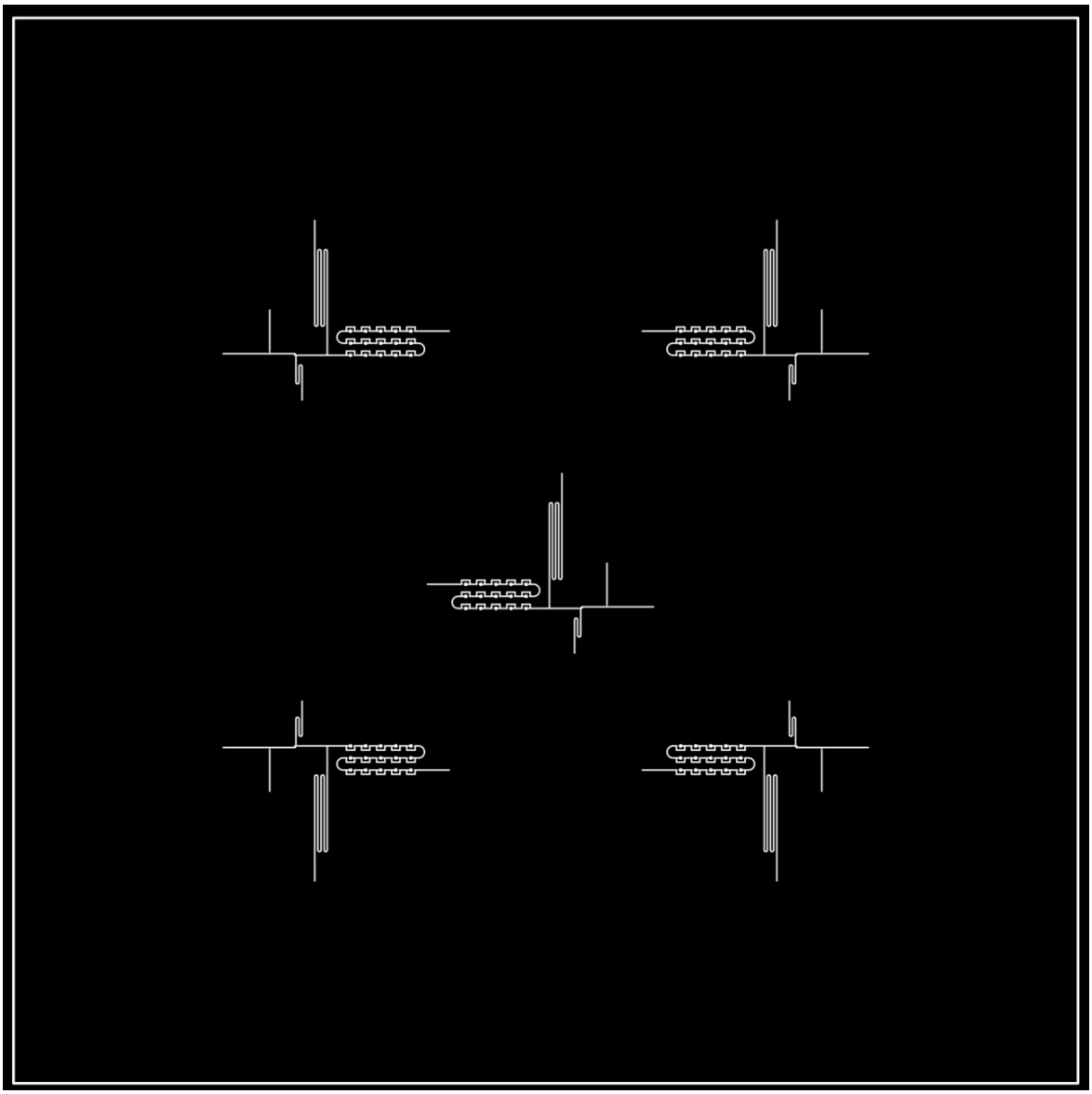

Figure 22. The schematic of mask

The design of droplet-based microfluidics is described in the citation [1]. In my experiment, we used the principle of direct trapping ($R_I < R_u$) to catch the cells (***Fig. 23***).

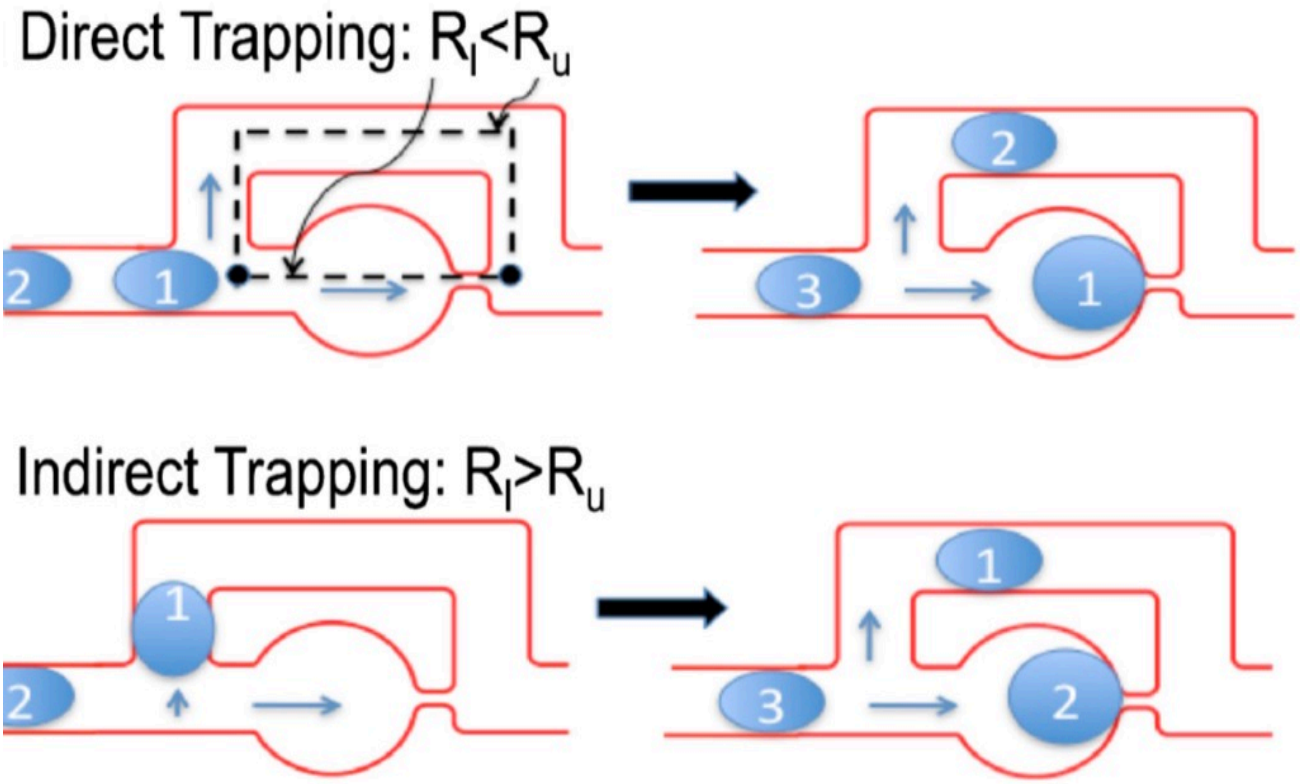

Figure 23. Droplet capture in the traps using direct trapping and indirect trapping approach

(a)

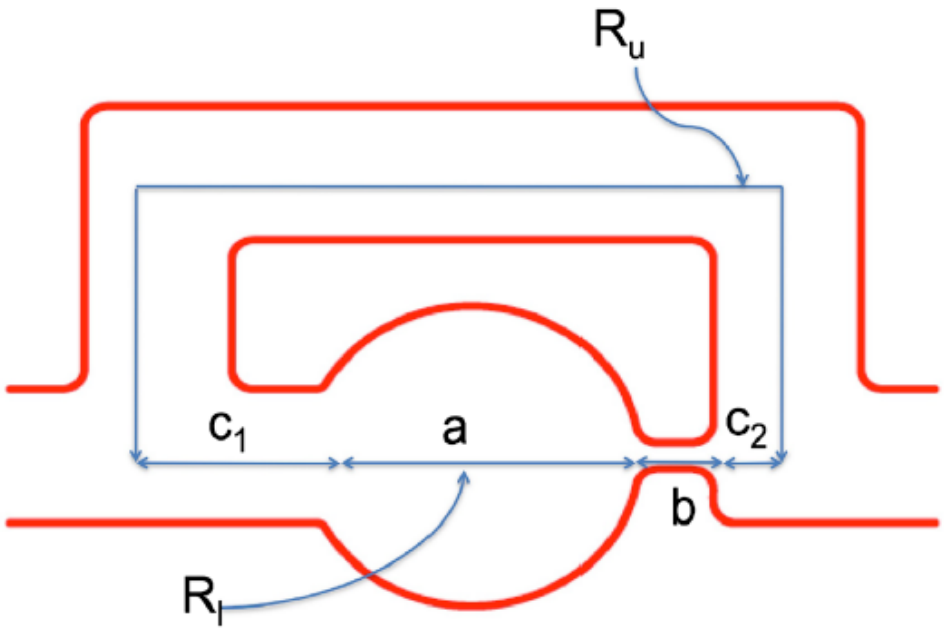

(b)

R_l/R_u	L_u, μm	L_a, μm	L_b, μm	L_{c1}, μm	L_{c2}, μm	W_u, μm	W_a, μm	W_b, μm	W_{c1}, μm	W_{c2}, μm	h, μm
0.19	7700	450	100	200	100	200	450	55	200	200	80
0.38	4500	450	100	200	100	200	450	50	200	200	80
1.56	1700	450	100	200	100	200	450	40	200	200	80
4.38	2100	450	400	200	100	200	450	40	200	200	80

Figure 24. (a) Schematic of a single loop highlighting the various geometric dimensions; (b) the table shows four different ratios of lower to upper branch resistance that were tuned by varying the width (w) and length (l) of the constriction in the hydrodynamic trap and the length of the upper branch. The subscripts denote the various sections of the feometry;

Here, both of the channel resistances (R_l and R_u) were calculated using the following equation:

$$R = \frac{12\mu L}{h^3 w}\left[1 - \sum_{n,odd}^{\infty} \frac{1}{n^5} \times \frac{192}{\pi^5} \times \frac{h}{w}\tanh\left(\frac{n\pi w}{2h}\right)\right]^{-1}$$

The ratio was tuned by varying the width and length of the constriction in the hydrodynamic trap and, the length of the upper branch as shown in ***Fig. 24.*** The trap size (w_a = 150 μm) and device height (h = 80 μm) were fixed. The data we used for our microfluidic device illustrated in ***Fig. 25.***

2nd generation				
Ru	Ra	Rc1	Rb	Rc2
0.000370826	2.73E-05	5.52E-05	0.003102939	1.57E-05
Sum RI				
0.003201051				
RI/Ru	If wb=10			
8.632217806	60			

Lu	La	Lb	Lc1	Lc2	Wu	Wa	Wb	Wc1	Wc2	h
1515	150	360	360	360	235	150	75	30	75	80

Figure 25.Parameter datasheet in the microfluidic device

APPENDIX C. MATERIALS AND SURFACE FUNCTIONALIZATION

Materials

1. 1/9 (mol ratio) of HSC10COOH/HSC8OH in absolute ethanol.
    a. Get 10 ml 0.2mM HSC10COOH:
        i. Take 4.3672mg in 10ml absolute ethanol to get 2mM HSC10COOH
        ii. 1 ml 2mM mix with 9ml absolute ethanol to get 0.2mM HSC10COOH
    b. Get 10 ml 1.8mM HSC8OH
        i. 31.4ul HSC8OH in 10ml to get 18Mm
        ii. 1ml 18mM HSC8OH, mix with 9ml absolute ethanol to get 1.8mM HSC8OH
    c. Mix 10ml 0.2mM HSC10COOH & 10ml 1.8mM HSC8OH
2. NHS and EDC
    a. 0.2M N-hydroxysuccinimide (NHS) and 0.05M N-(3-dimethylamnopropyl)-N-ethylcarbodiimide hydrochloride (EDC) in H_2O, 2.3018g NHS, 0.9585g EDC dissolve in 100ml H_2O
3. 1M PH8 phosphate buffer
    a. 1M Na_2HPO_4: 56.784g Na_2HPO_4 dissolve in 400ml H_2O
    b. 1M NaH_2PO_4: 11.998g NaH_2PO_4 dissolve in 100ml H_2O
    c. 1M pH8 phosphate buffer: 372.8ml 1M Na_2HPO_4 + 27.2ml 1M NaH_2PO_4
4. 0.1M pH7.2 PBS with 5mM KCl and 1mM
    a. 0.1481g KCl, 32g NaCl, 5.76g Na_2HPO_4, 0.96g KH_2PO_4, 0.08g $MgCl_2 \bullet 6H_2O$,

dissolve in 400ml H_2O, adjust pH using KOH.

5. 1M ethanolamine (EA) dissolved in H_2O
    a. 500µL EA dissolve in 9.401 H_2O

Surface functionalization protocol

1. Get a gold coated AAO sensor. Get the spectrum.
2. Dip HSC on the surface, incubate for overnight, 4 °C.
3. Rinse with Ethanol, then rinse with 10 mM PBS 8.0. Get the spectrum.
4. Dip EDC on the surface, incubate for 2 hours, room temperature.
5. Rinse with PBS 8.0. Get the spectrum.
6. Dip antibody on the surface, incubate for overnight, 4 °C.
7. Rinse with PBS 8.0. Get the spectrum. Dip EA on the surface, incubate for 2 hours
8. Rinse with PBS 8.0. Get dip A-beta or T-tau on the surface, incubate for 2 hours.
9. Rinse with PBS 8.0. Get the spectrum.

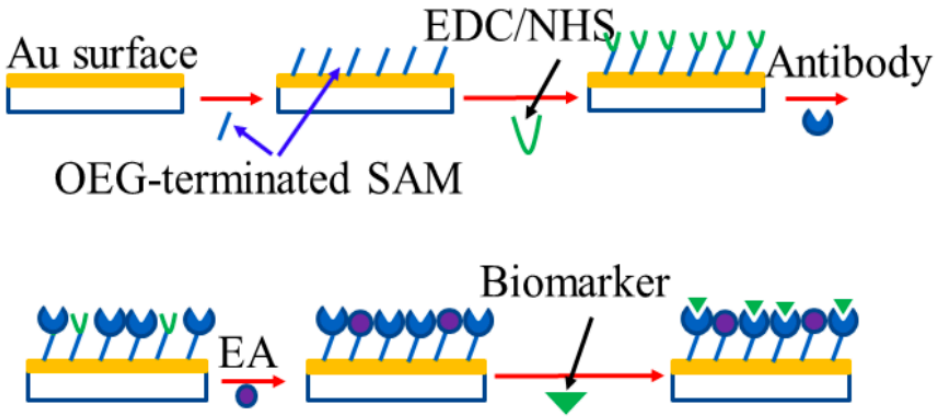

Figure 26. Surface functionalization flow

APPENDIX D. AAO FABRICATION

Materials

1. ITO glass (purchased from Nanocs, Inc). The sheet resistance is 100X/sq.
2. Photoresist (AZ1512) and AZ developer (purchased from AZ Electronic Materials).

Fabrication process

The fabrication process is described in ***Fig. 27a***. First of all, The ITO glass substrate need to be washed by DI water, Acetone, IPA, and DI water in sequence. After the ITO substrate being washed, it will be baked about 5 minutes to dry the surface. A thin film of aluminum layer is deposited by E-beam evaporation shown in ***Fig. 27b***. The quality of the aluminum layer is important to achieve the successful anodization. There are two requirements for this aluminum lay: 1. This layer should be totally oxide-free. 2. The surface should be smooth enough. Measurements have a typical roughness in the range of 6 − 12 nm [2-4]. Then, anodization process need to be applied. The processed glass will be added into the acid solution (0.3 M oxalic acid) with 45 V DC voltage at 2 C to form AAO (***Fig. 27c***). A layer of AAO will be formed over the substrate during this process. For the one-step anodization process [6], we only carry out one-step anodization on the samples for 25, 35, and 45 min. For the two-step anodization process [5], it takes 10 min for step-one anodization in 0.3 M oxalic acid, followed by etching using a mixture of phosphoric acid (0.4 M) and chromic acid (0.2 M) at 65 °C for 30 min, followed by a 40-minute step-two anodization in 0.3 Moxalic acid with the same experimental conditions as for step-one anodization. After the anodization process, another 150nm thick aluminum layer will be deposited on surface by the thermal evaporation as shown in ***Fig. 27d***. In order to create the nano pore on the AAO surface, a process of photolithography will be applied on the Al-coated AAO substrate.

For the photolithography process, we use the standard process designed by our research group: a 1 lm photoresist (AZ 1512) layer is spin-coated at 4000 rpm on the substrate, then the coated substrate is soft baked for 50 s at 95 °C. The micro-patterns are then transferred and generated on the photoresist through a photomask using a 416nm light exposure with a dose of 70 mJ/cm2, followed by a post-exposure bake for 50 s at 105 C. The exposed photoresist is developed and selectively removed by immersing in AZ developer for 25 s. The layer of AZ will protect the Al underneath to avoid being etched. The processed substrate will be added to the etching solution {(H3PO4: CH3-COOH: HNO3: H2O) 80:5:5:10 by weight%} for 35 s to etch away the Al layer ***Fig. 27e***. After that, the processed substrate will be added to a mixture of phosphoric acid (0.4 M) and chromic acid (0.2 M) at 20 C for 100 min to etch away the unprotected AAO ***Fig. 27f***. In the end, the rest of photoresist will be washed away by dipping the substrate in acetone, followed by removing the Al layer using the Al etching solution.

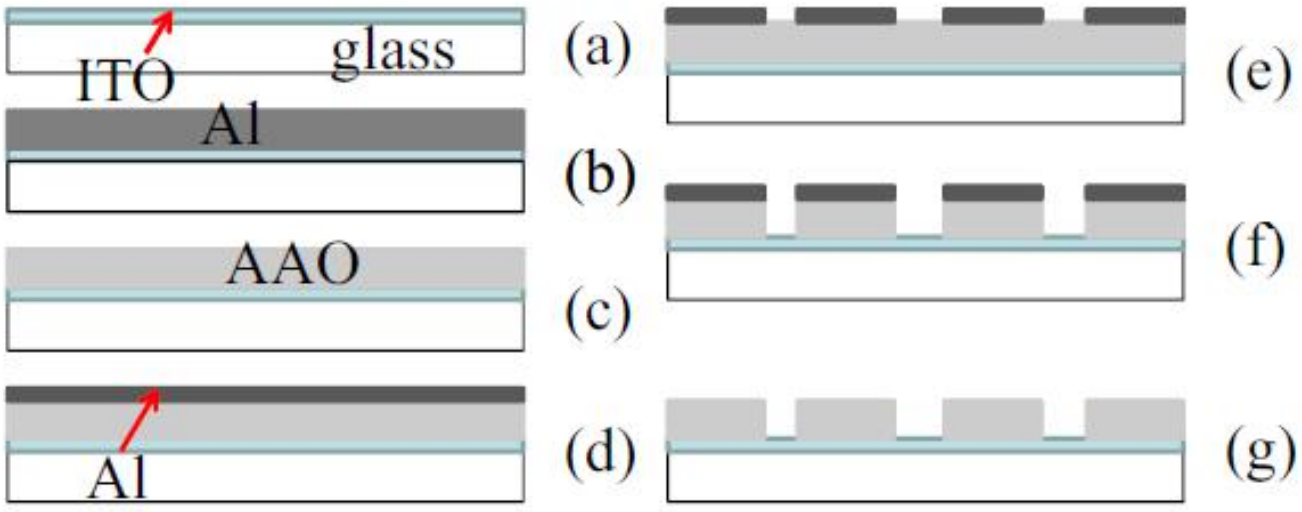

Figure 27. Sketch of the fabrication process flow for AAO micro-patterns

References

[1] Bithi, Swastika S., and Siva A. Vanapalli. “Behavior of a Train of Droplets in a Fluidic Network with Hydrodynamic Traps.” Biomicrofluidics, vol. 4, no. 4, 2010, p. 044110., doi:10.1063/1.3523053.

[2] X. Li, Y. He, T. Zhang, T. Lee, L. Que, Proc. IEEE NANO (2012), http://dx.doi.org/10.1109/NANO.2012.6321926.

[3] X. Li, Y. He, T. Zhang, L. Que, Opt. Express 20 (19) (2013) 21272–21277.

[4] X. Li, Y. He, L. Que, Langmuir 29 (7) (2013) 2439–2445.

[5] Y. He, X. Li, L. Que, J. Nanosci. Nanotechnol. 12 (10) (2012) 7915–7921.

[6] G. Sulka, S. Stroobants, V. Moshchalkov, G. Borghs, J.P. Celis, J. Electrochem. Soc. 149 (7)

(2002) 97–103.